analytical chemistry

pubs.acs.org/ac Article

Droplet-Based Microfluidic Temperature-Jump Platform for the Rapid Assessment of Biomolecular Kinetics

Tianjin Yang,[⊥] Alessia Villois,[⊥] Antonín Kunka, Fulvio Grigolato, Paolo Arosio,* Zbynek Prokop,* Andrew deMello,* and Stavros Stavrakis*

Cite This: *Anal. Chem.* 2022, 94, 16675−16684 Read Online

ACCESS | Metrics & More | Article Recommendations | Supporting Information

ABSTRACT: Protein folding, unfolding, and aggregation are important in a variety of biological processes and intimately linked to "protein misfolding diseases". The ability to perform experiments at different temperatures allows the extraction of important information regarding the kinetics and thermodynamics of such processes. Unfortunately, conventional stopped-flow methods are difficult to implement, generate limited information, and involve complex sample handling. To address this issue, we present a temperature-controlled droplet-based microfluidic platform that allows measurement of reaction kinetics on millisecond to second timescales and at temperatures between ambient and 90 °C. The utility of the microfluidic platform for measuring fast biomolecular kinetics at high temperatures is showcased through the investigation of the unfolding kinetics of haloalkane dehalogenases and the elongation of fibrils composed of the amyloid β peptide associated with Alzheimer's disease. In addition, a deep-ultraviolet (UV) fluorescence microscope was developed for the on-chip recording of protein intrinsic fluorescence spectrum originating from aromatic amino acid residues. We envision that the developed optofluidic platform will find wide applicability in the analysis of biological processes, such as protein refolding and phase separation.

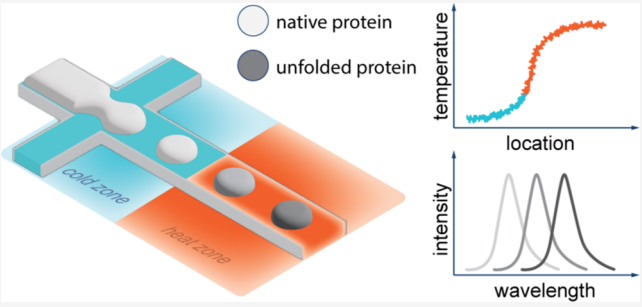

■ INTRODUCTION

A variety of studies in biochemistry and biophysics involve the investigation of biomolecular reactions that are characterized by rapid kinetics and dynamics. Examples include the measurement of protein and nucleic acid folding/unfolding,[1] enzyme catalysis,[2] ligand binding,[3] and protein−nucleic acid interactions.[4] In many situations, important information about the kinetics and more specifically the energetic and entropic contributions of a process can be elucidated by acquiring data at different temperatures. The success of this strategy relies on two critical factors; first, the rapid mixing of reagents to minimize the reaction dead times, and second, the ability to control temperature in an accurate and precise manner.[5] Indeed, coupling rapid reagent mixing with efficient temperature control has led to the realization of temperature-jump/stopped-flow[2] and laser-induced temperature-jump[6] platforms.

Commercial temperature-jump/stopped-flow instruments comprise a conventional stopped-flow module equipped with temperature controllers. Based on this approach, reaction volumes as small as 150 μL can be studied at temperatures between 20 and 70 °C, with a temperature jump of 5−50 °C and a dead time of between 2 and 5 ms (dependent only by the mixing efficiency of the instrument). Although temperature-jump/stopped-flow methods can provide a temperature jump as large as 50 °C, accessing different reaction temperatures necessitates variation of the ratio of hot to cold enzyme in a controlled manner, which in turn normally requires calibration prior to each experiment. Unsurprisingly, such an approach is poorly suited for high-throughput screening enzymatic kinetic profiles at multiple temperatures. Conventional laser-induced temperature-jump systems[6] generate temperature jumps up to 20 K within a few nanoseconds. By leveraging such fast heating capabilities, it is possible to monitor molecular kinetics or dynamics on nanosecond to microsecond timescales.[7] However, compared to stopped-flow/temperature-jump approaches, laser-induced temperature-jump systems are typically only able to generate relatively small temperature changes, and thus are limited to the study of protein dynamics that falls within these ranges.

The development of microscale mixing methods that leverage hydrodynamic focusing[8] chaotic advection[9] has been exceptionally useful for monitoring of the kinetics of rapid reactions. By reducing sample volumes to the nanoliter scale and using thermally conductive (gold-coated) microfluidic channels, Polinkovsky et al. were able to use lasers to heat

Received: July 12, 2022
Accepted: November 3, 2022
Published: November 17, 2022

Downloaded via ETH ZURICH on December 6, 2022 at 10:37:43 (UTC).
See https://pubs.acs.org/sharingguidelines for options on how to legitimately share published articles.

ACS Publications © 2022 American Chemical Society

https://doi.org/10.1021/acs.analchem.2c03009
Anal. Chem. 2022, 94, 16675−16684

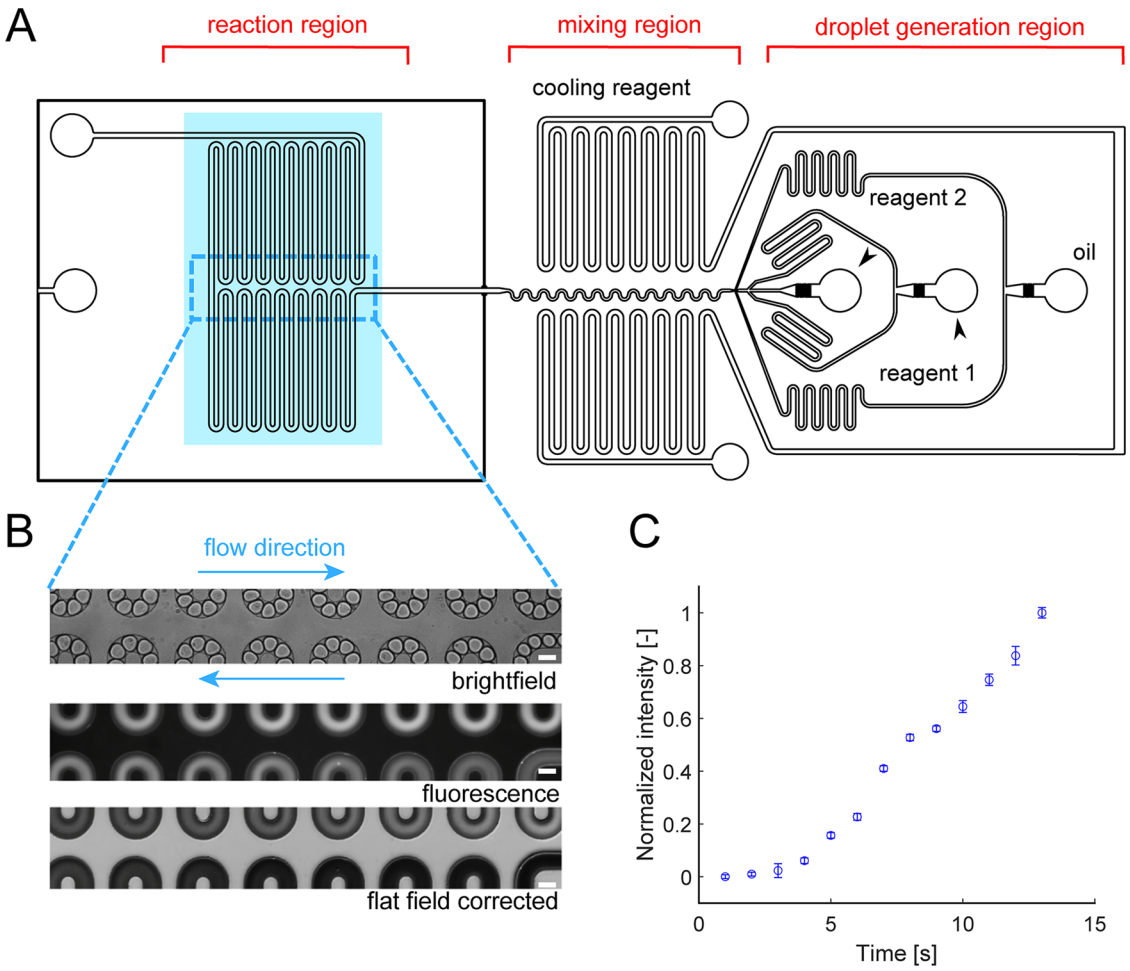

Figure 1. Parallel-channel microfluidic device. (A) Schematic of the parallel-channel microfluidic device, highlighting the integration of a flow-focusing droplet generator, a winding channel for efficient content mixing, and a reaction/heating loop region. The blue shaded area indicates the heating/reaction zone, and the region defined by the dotted blue rectangle represents the cropped area of the camera sensor used for detection. (B) Images of droplets moving along the reaction loop under bright-field and fluorescence imaging conditions and after flat-field correction of the fluorescence image. (C) Variation of ThT fluorescence intensity during insulin elongation as a function of position (time) along the flow path.

aqueous samples by 50 °C within 1 μs.[10] This allowed the folding and unfolding dynamics of DNA hairpins to be studied on microsecond timescales, with data indicating that complete folding and unfolding of DNA hairpins can be identified from the analysis of intermediate states between the folded and unfolded conformations. In addition to probing fast processes, it is also possible to use lasers to heat, cool, or control temperature on millisecond timescales, for in vivo monitoring of unfolding and refolding processes on timescales of several seconds.[11] Despite their undoubted utility, such microfluidic laser-induced temperature-jump approaches require the use of complex fabrication procedures and often the incorporation of sub-micron-depth microchannels.[10] Compared with conventional temperature-jump instruments, which require multiple heating steps to generate required temperature jumps, radiation-induced heating within microfluidic environments generates large temperature changes on extremely short timescales. Although such devices allow for efficient thermal transport, the manufacturing of sub-micron-scale features is complex, time-consuming, and demanding. Moreover, sub-micron channels are highly prone to blockage, readily adsorb analyte molecules on their surface, and require high applied pressures to move fluid.

In addition, all of the aforementioned temperature-jump microfluidic devices involve continuous hydrodynamic flows, which are undesirable when trying to minimize enzyme/substrate losses due to adsorption on channel surfaces.[12] Conversely, droplet-based microfluidic systems are ideally suited for performing reactions at controlled and elevated temperatures, due to the ease of generating small sample volumes and their ability to rapidly mix droplet payloads and vary payload composition in a rapid and robust manner.[13] Additionally, and significantly, the use of droplets in the presence of surfactants ensures negligible interaction of sample molecules with channel surfaces.[14] Typically, in water-in-oil emulsions, surfactant molecules act to decrease the interfacial tension and prevent subsequent coalescence of formed droplets. In this way, surfactants are able to control surface tension and ensure droplet stability that result in minimal cross-talk between droplets. Furthermore, since each droplet is isolated and independent of other droplets, large numbers of discrete experiments can be performed on short timescales, with a range of functional components being used to perform complex operations and workflows.[12]

We herein describe the development of a simple yet powerful microfluidic platform for measuring fast biomolecular kinetics over wide temperature ranges. Specifically, we describe

https://doi.org/10.1021/acs.analchem.2c03009
Anal. Chem. 2022, 94, 16675−16684

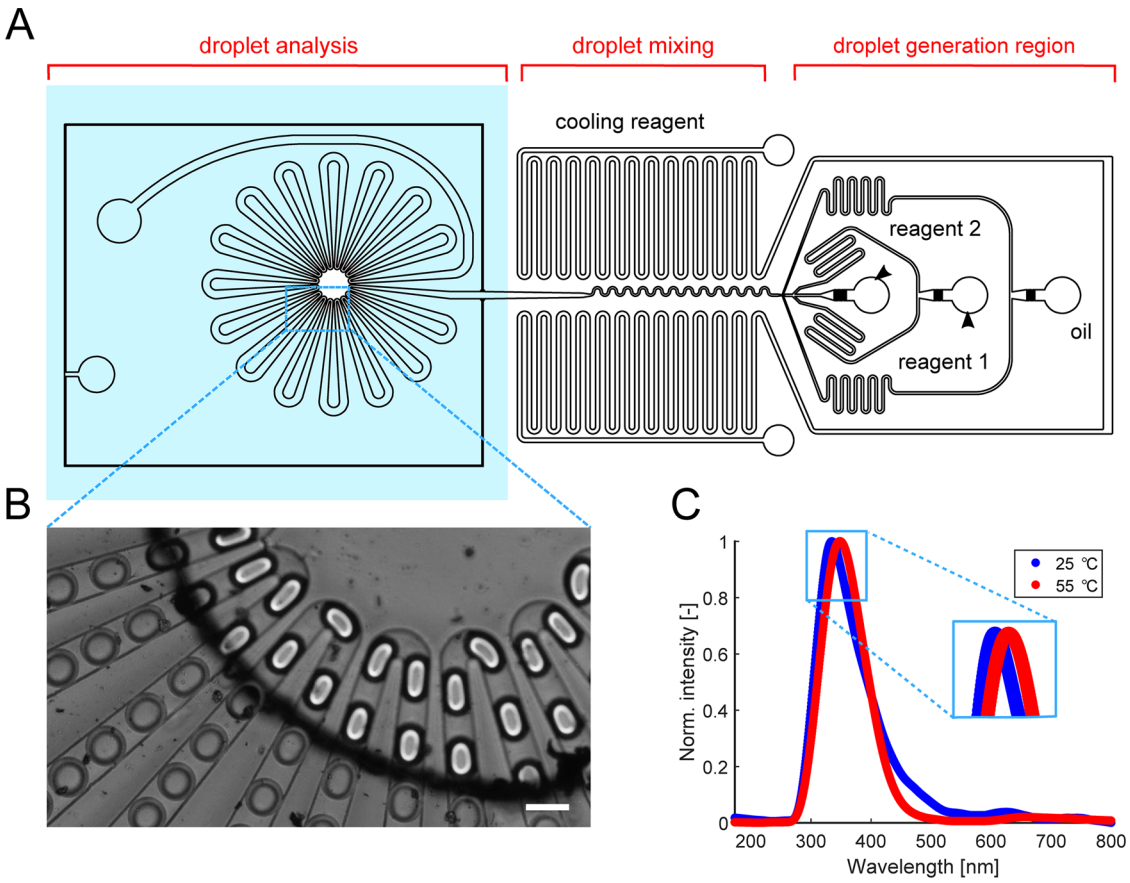

Figure 2. Radial-channel microfluidic device. (A) Schematic of the radial-channel microfluidic device, highlighting the integration of a flow-focusing droplet generator, a winding channel for efficient mixing, and a reaction/heating loop. The blue shaded area indicates the heating/reaction zone. A circular aperture is located at the center of the heating/reaction zone to enable facile optical interrogation of droplets moving along the microfluidic channel. (B) Bright-field images of 17 nL droplets moving inside the heating/reaction zone. Scale bar: 100 μm. (C) Fluorescence emission spectra of LinB using an excitation wavelength of 280 nm at two different temperatures. The observed redshift in the peak wavelength as temperature is increased from 25 to 55 °C indicates protein unfolding.

the operation of a droplet-based microfluidic system able to control the temperature between 25 and 80 °C, with a time resolution ranging from a few milliseconds up to 30 s. Rapid heat transfer (due to the large surface area-to-volume ratio of droplets) and the millisecond mixing timescale (due to efficient chaotic advection) minimize system dead times. Additionally, the use of a droplet-based format provides access to an extended time window that ranges from milliseconds to several seconds.[15] Finally, the device is compatible with deep-ultraviolet (UV) excitation and therefore with direct excitation of intrinsic fluorophores such as tryptophan (Trp), eliminating the need for substrate labeling with extrinsic probes.

To demonstrate the use of the microfluidic platform for measuring fast biomolecular kinetics at high temperatures, two exemplar systems were investigated. First, we studied the elongation of fibrils of amyloid β peptide, Aβ 1−42, implicated in Alzheimer's disease.[16,17] The development of assays capable of monitoring individual nucleation and growth steps is crucial in increasing our understanding of the aggregation process,[18] as well as interrogating the mode of action of potential drug molecules.[19] Specifically, we measured the kinetics of the growth of amyloid Aβ 1−42 fibrils over a period of 16 s under conditions that allow the analysis of elongation reactions and extracted the enthalpic and entropic contributions of the elongation reaction, consistent with previously reported bulk measurements[20,21] In a second application, we investigated the unfolding kinetics of haloalkane dehalogenase (HLD) LinB from *Pseudomonas paucimobilis* UT26.[22] More than three decades of experimental and in silico research on HLDs have made them benchmark enzymes for studying structure−function relationships (of >100.000 members of the α/β-hydrolase superfamily)[23] and the development of the novel rational approaches in protein engineering.[24−26] Understanding the (un)folding process offers several advantages in protein design such as improving stability,[27] identifying motifs or regions of a protein that are critical to functioning as potential drug targets,[28] or identifying mechanisms for misfolding or aggregation of proteins.[29] Recently, numerous reports have highlighted the importance of kinetic determinants in protein stability or aggregation susceptibility.[30,31] Herein, we demonstrate the use of a microfluidic platform to study protein unfolding kinetics by recording intrinsic protein fluorescence spectra as a function of time and temperature.[32] To analyze fluorescence spectra, we used global numerical data analysis combined with singular value decomposition. Both microfluidic platforms allow a time-resolved and spectral analysis of reaction progress at precise temperatures and thus represent useful tools for monitoring rapid biomolecular reactions.

■ RESULTS AND DISCUSSION

Working Principle and Methodology. The schematic representations of the microfluidic reactors used herein are

https://doi.org/10.1021/acs.analchem.2c03009
Anal. Chem. 2022, 94, 16675−16684

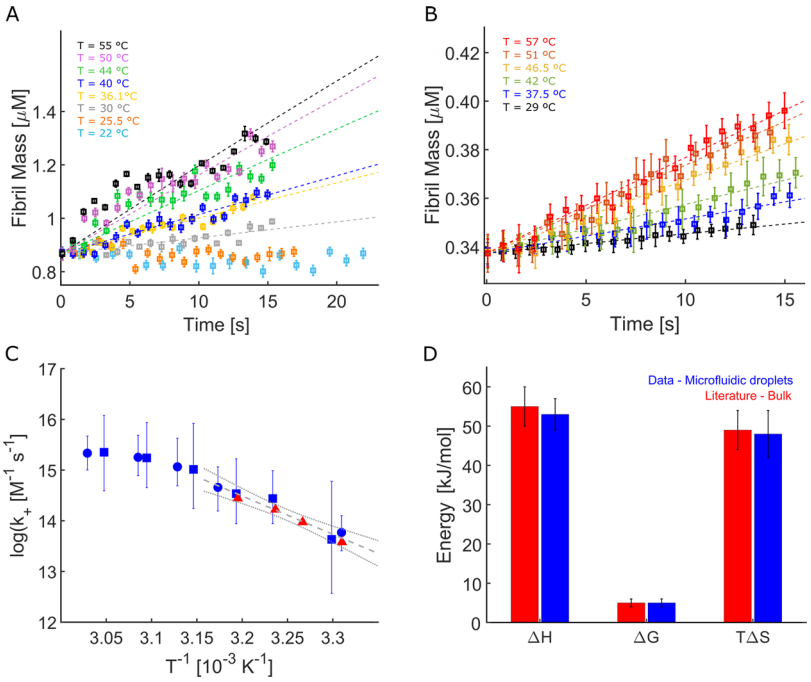

Figure 3. Analysis of the temperature dependence of amyloid β 1−42 fibril elongation rate using the microfluidic temperature-jump platform. Time evolution of the total fibril mass measured by monitoring ThT fluorescence in droplets containing (A) 8.7 μM and (B) 3.4 μM monomeric Aβ 1−42 at temperatures between 22 and 57 °C. Dotted lines represent the fitted curves for each temperature. (C) Arrhenius plot of the logarithm of the fibril elongation rate constant as a function of reciprocal temperature measured using the microfluidic temperature-jump platform (blue data points) and microplate experiments[20] (red data points). It should be noted that the blue circles and squares represent two independent (microfluidic) data sets. (D) Enthalpic and entropic contributions to the free energy of activation of the elongation rate, as measured using the microfluidic temperature-jump platform (blue) and microplate experiments (red). Error bars represent the standard errors of three measurements.

presented in Figures 1A and 2A. The polydimethylsiloxane (PDMS) device shown in Figure 1A,B is defined as the "parallel-channel device", and the device in Figure 2A,B is defined as the "radial-channel device". Both devices integrate an indium tin oxide (ITO)-coated glass slide that allows the temperature to be varied between 25 and 100 °C in a rapid and controllable manner. The parallel-channel device is composed of three regions: in the first region, monodisperse water-in-oil droplets of user-defined size are generated. The reactants inside the droplets are mixed by chaotic advection as they pass through a winding channel (mixing region). After mixing is complete, droplets enter the reaction (heating) zone, in which the reaction is triggered by a rapid increase in temperature. In the case of the parallel-channel device, the progress of the reaction is monitored by acquiring fluorescence images in the detection area (Figure 1A, blue rectangle). In this regard, it should be noted that a flat-field correction is used to eliminate artifacts caused by uneven illumination. This approach allows for the high-throughput monitoring of fluorescence at multiple positions, that correspond to different reaction time points (Figure 1B). Figure 1C shows fluorescence intensity data for Thioflavin T (ThT) as a function of time along the reaction zone. In this case, the increase of the fluorescence signal of the ThT dye reports the elongation of insulin amyloid fibrils (see the Experimental Section). The temperature inside the device was evaluated using the pH-sensitive dye 8-hydroxypyrene-1,3,6-trisulfonic acid (HPTS) (see Supporting Text 1 for details and Figure S1). In addition, and as shown in Figure S2, we evaluated two critical parameters of the heating platform: the time that a droplet spends within the temperature gradient before entering the reaction zone and the time required by the droplet to thermally equilibrate after entering the reaction zone. According to this analysis, the equilibration time of droplets in the reaction zone at various set temperatures is on the scale of a few milliseconds.

Amyloid β 1-42 Fibril Elongation Kinetics. As a first application, we assessed the growth of amyloid fibrils of the peptide abeta1−42 (Aβ 1−42), which is strongly associated with the onset and progression of Alzheimer's disease.[33] We measured the kinetics of amyloid growth via a droplet assay that monitors ThT fluorescence;[34] a common quantitative reporter of the formation of β sheet-structures of amyloid aggregates.[35] The formation and growth of amyloid fibrils result from a complex reaction network consisting of several microscopic steps of nucleation and growth.[36] We designed our assay to specifically probe the fibril elongation rate and neglect the contribution of additional fragmentation and nucleation events. To this end, we added a high concentration of preformed fibrils (10% in monomer equivalent) to monomeric solutions of the peptide, which enables the bypass of nucleation events.[20,37,38]

We initially measured the elongation kinetics of Aβ 1−42 fibrils at the reference temperature of 37 °C and at different monomer concentrations (Figure S3). The composition of the reagent mixture in each droplet was 1.83, 3.87, or 7.33 μM of monomeric Aβ 1−42, with 10% fibrils (monomer equivalent) and 6 μM ThT; 120 μm diameter droplets were formed at 57 Hz with a velocity of 6.9 mm/s, as determined from bright-field images. This velocity yields a time interval of 1 s between each measurement point, and a total kinetic time window of 16 s. At each point, a total of 200 images were recorded (with an exposure time of 500 ms), corresponding to the analysis of 5730 droplets. As can be seen in Figure S3, fluorescence intensity increases as a function of time (along the length of

https://doi.org/10.1021/acs.analchem.2c03009
Anal. Chem. 2022, 94, 16675−16684

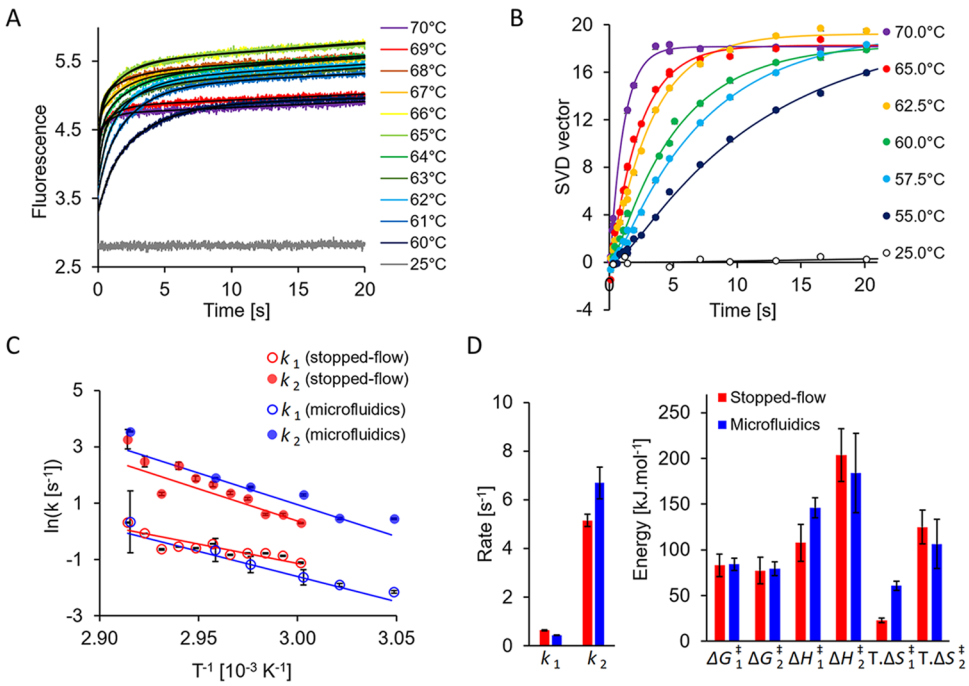

Figure 4. Unfolding kinetics of LinB analyzed by conventional and microfluidic temperature-jump techniques. (A) Kinetic traces recorded using conventional stopped-flow/temperature-jump instrumentation at temperatures ranging from 60 to 70 °C. Each curve is an average of three individual measurements, with the solid lines representing a double-exponential fit to individual traces. (B) SVD amplitude vectors calculated from the time-resolved spectra obtained with the microfluidic temperature-jump platform at different temperatures. It should be noted that each SVD data point represents a whole spectrum. Solid lines represent the best global fit to the entire microfluidic data set. (C) Arrhenius plot describing the temperature dependence of the fast (red filled circles) and slow (red empty circles) rates obtained by stopped-flow analysis. The red solid line represents the linear fit weighted by the standard errors of the rate estimates (error bars). The temperature dependence of the fast (blue filled circles) and slow (blue empty circles) rates were obtained by individual analysis of microfluidic time-resolved spectra at each temperature. Solid blue lines are the projection of the temperature dependence of rate constants obtained by global fitting. (D) Comparison of the rate constants and thermodynamic parameters obtained by stopped-flow (red) and microfluidic (blue) analysis (reference temperature = 338.15 K). The error bars represent the standard errors of the nonlinear fit to the stopped-flow data and standard errors in the microfluidc measurements were estimated during global fit of the microfluidic data.

the microfluidic channel) and reports fibril mass growth at 37 °C. The growth of Aβ 1−42 fibril mass over time was consistent with the predictions originating from a model based on mass conservation, which describes the elongation of fibrils by monomer addition according to

$$\frac{d[M(t)]}{dt} = 2k_+[m(t)][P(t)] \quad (1)$$

where $[M(t)]$ denotes the fibril mass concentration, t is the time, $[P(t)]$ is the fibril number concentration, $[m(t)]$ is the soluble monomer concentration, and k_+ is the elongation rate constant.[20] Experimental data were accurately described by model simulations (see the Experimental Section) with an elongation rate constant of $k_+ = 3 \times 10^6\ M^{-1}\ s^{-1}$, a value which is in excellent agreement with previous measurements performed in bulk.[20]

We next evaluated the temperature dependence of the elongation rate by measuring the aggregation of 8.7 μM (Figure 3A) and 3.4 μM (Figure 3B) monomeric Aβ 1−42 solutions in the presence of 10% (monomer equivalent) seeds, at temperatures between 22 and 57 °C. The temperature dependence of kinetic rate constants can be linked to the corresponding free-energy activation barrier, $\Delta G^{\ddagger}$, where $\log(k) = \log(A) - (\Delta G^{\ddagger}/(RT))$, with a suitable prefactor A. The use of the thermodynamic identity $\Delta G^{\ddagger} = \Delta H^{\ddagger} - T\Delta S^{\ddagger}$ enables computation of both the enthalpic ($\Delta H^{\ddagger}$) and entropic ($\Delta S^{\ddagger}$) components of $\Delta G^{\ddagger}$ starting from experimental measures of k_+ as a function of temperature T. Figure 3C reports the Arrhenius plot for the k_+ values estimated between 29 and 57 °C. Between 29 and 42°C the elongation rate increases linearly with temperature. Indeed, a linear fit in this range provided thermodynamic parameters that are in excellent agreement with bulk elongation data available in the literature,[18] and shows a small free-energy barrier of $\Delta G^{\ddagger}$ = (5 ± 1) kJ/mol (Figure 3D). This free-energy value results from an enthalpic barrier of $\Delta H^{\ddagger}$ = (53 ± 4) kJ/mol and a favorable entropic component of $T\Delta S_{37°C}^{\ddagger}$ = (48 ± 6) kJ/mol. A statistical analysis, based on Welch's t-test, was performed by calculating the p values of the thermodynamic properties between those reported in the literature values and those obtained using the microfluidic method (Figure 3D). As observed in Table S1, there is no statistically significant difference between these values, with p-values being more than 0.05.

The enthalpic barrier has been related to the rearrangement of the hydrogen bonds and structure of the Aβ 1−42 peptide upon solvation, while the favorable entropy of activation has been attributed to the desolvation of hydrophobic regions of Aβ 1−42 monomers added to the ends of fibrils. The elongation rate plateaus at temperatures higher than 42 °C, denoting the appearance of temperature dependence in the $\Delta H^{\ddagger}$ and $\Delta S^{\ddagger}$ values for fibril elongation. To describe this temperature dependence, we introduced a change in the heat capacity ($\Delta c_p^{\ddagger}$) in the model (see the Experimental Section).

https://doi.org/10.1021/acs.analchem.2c03009
Anal. Chem. 2022, 94, 16675−16684

This new analysis was able to describe the experimental data over the entire temperature range, considering a negative change in the heat capacity value, $\Delta c_p^{\ddagger} = (-1.1 \pm 0.5)$ kJ/(mol·K). This is consistent with the previous finding that the hydrophobic effect is responsible for the stabilization of the fibril structure, which leads to a favorable entropy of activation.[39] Taken together, these results highlight the power and reliability of the temperature-controlled microreactor for monitoring the rapid kinetics associated with fibril elongation on the millisecond to second timescales, and for accessing thermodynamic signatures of kinetic activation barriers with minimal sample consumption. This, in turn, provides valuable insights into the microscopic mechanisms that drive the aggregation process.

Unfolding Kinetics of Haloalkane Dehalogenase LinB. We next sought to apply our platform to the study of haloalkane dehalogenase LinB unfolding, using the intrinsic fluorescence of the aromatic residues within the enzyme. This was accomplished by acquiring fluorescence emission spectra at distinct positions (inner loops) inside the aperture of the ITO-coated glass slide; highlighted by the dashed rectangle in Figure 2A and displayed in Figure 2B. The radial PDMS device in Figure 2B was used for the deep-UV unfolding experiments since a circular aperture in the ITO layer could be fabricated in a direct manner and allowed for efficient coupling of the excitation light into the microfluidic channel. Droplets are formed using a flow-focusing geometry, with a downstream serpentine channel section being used to ensure rapid mixing inside each droplet. To allow for data collection at different time points, the microfluidic device integrates several interrogation points (channel loops). Detection occurs in the radial channel after the droplet has entered the heating zone. To quantify the progress of a reaction at different time points, we accurately align each channel loop with the optical probe volume in a sequential manner. The microfluidic device allows for observation times over a period of 20 s. Trp fluorescence detection was achieved using deep-UV excitation, a UV−visible (UV−vis) spectrometer, and an EMCCD camera (Figure S4). Importantly, the PDMS substrate is transparent at 280 nm and exhibits minimal fluorescence, thus allowing efficient detection of Trp emission at 350 nm. The use of the EMCCD camera allows verification of the position along the microfluidic channel where each emission spectrum should be acquired. At each position, 100 separate spectra were acquired and then averaged to enhance signal-to-noise ratios. It is important to note that measurement of the whole spectrum is crucial in allowing the deconvolution of the protein unfolding process from the effect of temperature on Trp emission. Here, an increase in temperature leads to a decrease in the Trp emission, while shifts toward higher wavelengths are associated with protein unfolding.[40] Acquisition of the whole emission spectrum allows the decoupling of these two effects, a task that is not possible through analysis of the time-integrated fluorescence intensity. Figure 2C presents fluorescence emission spectra of LinB Trp residues acquired using our microfluidic device at 25 and 55 °C, highlighting a characteristic redshift when the protein undergoes thermally induced unfolding.

Prior to microfluidic-based experimentation, we evaluated the kinetics of LinB unfolding using a conventional stopped-flow temperature-jump apparatus (Figure 4A). Here the unfolding of LinB was studied by measuring fluorescence emission variations at 11 different temperatures between 60 and 70 °C. Kinetic traces were fitted to a double-exponential function (eq 2)

$$y = A_{\text{fast}} \cdot e^{-k_{\text{fast}} \cdot t} + A_{\text{slow}} \cdot e^{-k_{\text{slow}} \cdot t} + B \cdot t + C \tag{2}$$

where y is the fluorescence intensity at time t, A_{fast} and A_{slow} are the amplitudes, and k_{fast} and k_{slow} are rates of the fast and slow phases, respectively. Two additional parameters B and C account for the linear drift of the observed signal and the signal offset, respectively. Next, the extracted reaction rates (k) were fitted to the Arrhenius and Eyring equations (see the Supporting Information, Methods) to estimate the thermodynamic parameters E_a and $\Delta G^{\ddagger}$, $\Delta H^{\ddagger}$, $\Delta S^{\ddagger}$ for both kinetic phases (Figure 4C,D and Table S2).

The double-exponential nature of the stopped-flow data indicates a two-step mechanism involved in the unfolding pathway (eq 3), where N, I, and D are the native, intermediate, and denatured forms, respectively, and k_1 and k_2 are the rate constants of the component steps.

$$N \xrightarrow{k_1} I \xrightarrow{k_2} D \tag{3}$$

However, such an analysis cannot properly assign an experimentally observed phase (Figure 4A) to either the first (k_1) or second kinetic step (k_2) in the unfolding kinetic pathway (for a detailed discussion see Supporting Text 2). The two phases described by the stopped-flow data indicate that the intermediate species significantly contributes to the fluorescence signal. Interestingly, our model simulation showed that initial formation of the intermediate I is always fast and followed by a slow decay (Figure S5), regardless of whether the first step (k_1) in the reaction pathway (eq 3) is fast or slow. To better understand the contributions of individual species to the stopped-flow fluorescence signal we adopted the following experimental workflow. First, we monitored Trp emission spectra as a function of time for various temperature conditions (Figure S6). Second, we performed temperature denaturation experiments (temperature scans from 20 to 80 °C) using static light scattering (SLS) and circular dichroism (CD) analysis (Figure S7). Finally, we combined the information from both these studies with simulations of the evolution of the fluorescence signal during unfolding (Figure S8 and Supporting Text 2). Although this workflow was successful at revealing the origin of the kinetic sequence (eq 3), it is laborious, time-consuming, and consumes excessive amounts of valuable protein.

The combination of the microfluidic temperature-jump platform with whole spectra acquisition provides an optimal approach to overcome the aforementioned limitations when studying temperature-induced protein unfolding. We used the platform to record the LinB (Trp) emission spectra as a function of time and at different temperatures. A protein concentration of 1 mg/mL was used in all experiments (matching the concentration used in the conventional stopped-flow temperature-jump study), and droplet velocities were varied between 11 and 214 mm/s, depending on the flow rate and the position in the channel, corresponding to reaction times between 0.06 and 20 s. The raw emission spectra are depicted in Figure S9. To analyze the complex microfluidic data set, we used a combination of singular value decomposition (SVD) and numerical integration of rate equations. This methodology has recently been used with some success to globally analyze time-resolved spectra when studying the mechanism of a "declick" chemical reaction.[41]

https://doi.org/10.1021/acs.analchem.2c03009
Anal. Chem. 2022, 94, 16675−16684

Herein, we extended this methodology to the analysis of time-resolved spectra collected over a range of temperatures, providing a mechanistic and thermodynamic understanding of the protein unfolding pathway. Initially, the individual time-dependent spectra were resolved by SVD analysis. The extracted SVD amplitude vectors were then fitted numerically (Figure 4B) to a "minimal" kinetic model proposed for LinB unfolding (eq 3, and Experimental Section). Numerical analysis of the time-resolved spectra enabled the extraction of a unique solution to the kinetic mechanism of LinB unfolding by providing a single set of kinetic constants and energy barriers (Figure 4C and Table S2). In addition to conventional regression analysis, global analysis of "on-chip" data allows a rigorous analysis of the variance; reported herein as confidence contour analysis.[42] Such an analysis confirms the high quality of the global fit, with all obtained kinetic and thermodynamic parameters being well constrained by the experimental data (Figure S10). The results of the global fit and the obtained estimates for the rate constants and thermodynamic parameters are summarized in Figures 4C,D and S9 and S10 and Table S2. Data resulting from the stopped-flow and microfluidic experiments exhibited a similar temperature dependence of the rate constants (Figure 4C) as well as comparable thermodynamic parameters (Figure 4D) for the activation barriers of the two steps in the kinetic pathway. In both steps, the free energy of activation ($\Delta G^{\ddagger}$) consists mainly of the activation enthalpy ($\Delta H^{\ddagger}$), which is compensated by a favorable activation entropy ($T\Delta S^{\ddagger}$), especially for the second step (k_2). The strong enthalpy/entropy compensation observed for k_2 step is most likely caused by the rearrangement of water molecules and the desolvation of exposed hydrophobic residues associated with LinB aggregation. A Welch's *t*-test (Table S1), was performed on the unfolding thermodynamic data extracted from stopped-flow and microfluidic measurements (Figure 4D) and indicated no significant differences (p-values > 0.05), except the value of $T\Delta S^{\ddagger}$ for the k_1 step which shows a p-value slightly smaller than 0.05.

Compared to conventional stopped-flow experiments, the ability to acquire spectral data via our microfluidic method provides significant advantage when assigning the origin of the steps involved in the temperature-induced unfolding of LinB. Indeed, LinB provides an attractive example of kinetic stability, where a large initial barrier separates the native state of the enzyme from its transition to degradation products. This initial kinetic barrier guarantees that the biological function of the enzyme is maintained, even if the native state is not thermodynamically stable.[30] In this regard, the rapid heating capability of the microfluidic platform combined with emission spectrum acquisition is invaluable in extracting kinetic parameters and provides important information when designing stable enzymes for biotechnological applications.[43,44]

■ CONCLUSIONS

Herein, we have developed a droplet-based microfluidic platform for monitoring fast kinetic processes at elevated temperatures, on millisecond-to-second timescales, and integrating temperature jumps as large as 55 °C. Significantly, the dead time of the platform is only a few milliseconds and can be controlled by the variation of droplet volumes and velocities, with the use of pL-volume droplets significantly reducing accessible dead times.

To showcase the efficacy of the platform in probing fast biological processes, we studied the elongation kinetics of Aβ1−42 fibrils at different temperatures and over a time window of 16 s. Data are in excellent agreement with kinetic parameters reported in the literature and additionally allow for an accurate assessment of the thermodynamic signatures underlying the activation barrier. Acquiring kinetic data at different temperatures provides information on activation energies that drive the aggregation process and this information can be potentially used for the design of potential drugs.

The temperature-induced unfolding of LinB was analyzed using the microfluidic platform and compared to data extracted via conventional temperature-jump/stopped-flow apparatus. The presented results demonstrate the suitability of the microfluidic platform in studying fast kinetic processes. Specifically, the high surface-to-volume ratios associated with the microfluidic channels ensure that heat and mass transfer can equilibrate local temperatures within a few milliseconds of the droplets entering the heating zone. By virtue of such rapid equilibration, fluorescence spectra may be acquired during the unfolding process, capturing the thermally induced onset of the transition. Accordingly, and in contrast to conventional temperature-jump methods, microfluidic temperature-jump measurements can be conducted without laborious calibration prior to data collection. To our knowledge, this is the first time that such an approach has been applied to whole spectra kinetic analysis with a view to gaining mechanistic and thermodynamic insight into the protein unfolding pathway. Additionally, the protein unfolding parameters obtained by global fitting of the kinetic data (from conventional temperature-jump/stopped-flow experiments) in conjunction with temperature denaturation experiments (see the Supporting Information) were consistent with values obtained from the microfluidic platform. Accordingly, the microfluidic measurements in combination with global data analysis made it possible to unambiguously identify the individual steps involved in the unfolding pathway, which otherwise cannot be discriminated from stopped-flow data. The platform also provides for label-free detection. The device is versatile and can be easily adapted to many applications (through rapid prototyping and integration with existing laboratory equipment), such as the study of crystal nucleation kinetics after a temperature quench or the study of the kinetics of protein phase transitions across wide temperature ranges.

It should be noted that it is typically not simple to isolate transient intermediates during temperature-induced unfolding experiments. In this respect, the generation of time-resolved spectra is highly advantageous compared to intensity time data when extracting quantitative information from multiple species. SVD analysis of time-resolved spectra is adept at revealing the underlying spectra and the time dependencies of each species over a range of concentrations or temperatures. Additionally, the combination of SVD and numerical integration analysis overcomes the limitations of conventional fitting methods when fitting data to multiple exponentials.[2,41] By choosing an appropriate probe and detection method, it is clear that our microfluidic platform can also be used to study both enzyme kinetics and protein stability at elevated temperatures.

■ EXPERIMENTAL SECTION

Amyloid β 1−42 Fibril Elongation Kinetics. Experiments assessing the concentration dependence of elongation rate were performed as follows. Three concentration pairs of

https://doi.org/10.1021/acs.analchem.2c03009
Anal. Chem. 2022, 94, 16675−16684

Aβ 1−42 monomers (14.6, 7.8, 3.6 μM) in the presence of 10% (monomer equivalent) seeds were mixed on chip to induce Aβ 1−42 fibril elongation. In all cases, Thioflavin T was introduced in the fibril solution at a concentration of 12 μM. The monomer and fibril solutions were introduced into two different reagent inlets at an equal flow rate of 1 μL/min, together with an oil flow rate of 1 μL/min. This yielded final concentrations of 7.3, 3.9, 1.8 μM for Aβ 1−42 monomers, and 6 μM for ThT (Figure S3). Experiments assessing the temperature dependence of fibril elongation rates were accomplished by measuring aggregation in 8.7 and 3.4 μM monomeric Aβ 1−42 solutions in the presence of 10% (monomer equivalent) seeds.Once droplets were formed, they entered the heating zone where reaction initiation occurs at 37 ± 0.2 °C. A 2048 × 300-pixel region of interest (ROI) was cropped along the serpentine channel and used to monitor the reaction (blue rectangular frame in Figure 1A). Fluorescence measurements at each concentration were obtained using a 500 ms exposure time, with 200 images being recorded. The acquired fluorescence images were flat-field corrected (described in detail below), normalized, and after a position-to-time conversion within the ROI, the kinetics of the fibril elongation reaction were obtained.

Equation 4[45] was used to fit the Arrhenius data over the entire temperature range and describes the elongation rate constant as a function of the corresponding free-energy barrier $\Delta G^{\ddagger}$, i.e.

$$k_+ = 10^3 \cdot D \cdot N_A \cdot r_{eff} \cdot e^{-\beta \Delta G^{\ddagger}} = 10^3 \cdot D \cdot N_A \cdot r_{eff} \cdot e^{-\beta \Delta H^{\ddagger}} e^{\beta T \Delta S^{\ddagger}} \tag{4}$$

Here, D is the diffusion constant of a segment of the protein, N_A is Avogadro's number, β is the reciprocal of the thermodynamic temperature of a system $(1/k_B T)$, $\Delta H^{\ddagger}$ is the enthalpic barrier, $T\Delta S^{\ddagger}$ is the entropic contribution to the free energy of activation, and r_{eff} is a characteristic distance given by

$$r_{eff} = \frac{b_0}{\pi\sqrt{2n}} \tag{5}$$

where b_0 is the Kuhn length of a polypeptide chain and n is the number of Kuhn segments.[5] By considering changes in the heat capacity, $\Delta c_p^{\ddagger}$, to both enthalpy and entropy, expressions for $\Delta H^{\ddagger}$ and $\Delta S^{\ddagger}$ can be generated, i.e.

$$\Delta H^{\ddagger} = \Delta H^{\ddagger}_{T_{ref}} + \Delta c_p^{\ddagger}(T - T_{ref}) \tag{6}$$

$$\Delta S^{\ddagger} = \Delta S^{\ddagger}_{T_{ref}} + \Delta c_p^{\ddagger}(\log T - \log T_{ref}) \tag{7}$$

For a reference temperature T_{ref} (chosen to be 310 K), this yields

$$\log(k_+) = \log\left(\frac{10^3 k_B N_A b_0}{6\pi^2 \eta r \sqrt{2n}}\right) - \log(\tilde{T}) - \frac{\Delta H_{37°C}}{k_B}\tilde{T} - \frac{\Delta c_p^{\ddagger}}{k_B}(1 - \tilde{T}T_{37°C}) + \frac{\Delta S^{\ddagger}_{37°C}}{k_B} - \frac{\Delta c_p^{\ddagger}}{k_B}(\log(\tilde{T}) + \log(T_{37°C})) \tag{8}$$

where η is the viscosity of the system.

Kinetics of LinB Unfolding via On-Chip Analysis of Emission Spectra. For LinB unfolding experiments, spectra were acquired at different positions along the reaction path and within the circular aperture of the ITO-coated glass. For each position of interest, 100 spectra were acquired once the temperature was equilibrated and averaged. Time-resolved spectra collected on-chip were fitted and analyzed using KinTek Explorer (KinTek Corporation, Snow Shoe). This software package is a dynamic kinetic simulation program that allows multiple data sets to be analyzed simultaneously using a single model.[46] The model was input through simple text descriptors and the program derived differential equations needed for numerical integration automatically. Experiments performed at 25, 55, 57.5, 60, 62.5, 65, and 70 °C were simultaneously fit to known spectra of native LinBwt. The time-resolved spectra were resolved by SVD analysis integrated within KinTek Explorer. Extracted SVD amplitude vectors were then fitted to a proposed two-step kinetic model by nonlinear regression analysis based on the numerical integration of rate equations. Values obtained from stopped-flow measurements as well as rate constants, and energy barriers were used as starting parameters in the numerical integration. The spectra of native LinB collected at room temperature were used as a reference to reduce the number of variables in the fitting procedure. Alternating between fitting of SVD amplitude vectors and the direct fitting of spectra helped us in finding the best global fit to the data. Both scenarios, where either the first step of the pathway k_1 or the second step k_2 is fast or slow, were tested during global fitting. The results from these simulations showed that in both cases the initial step is slow and the second step fast. Data fitting searched a set of parameters using the Bulirsch−Stoer algorithm with an adaptive step size that produces a minimum χ^2 value via nonlinear regression based on the Levenberg−Marquardt method. Residuals were normalized by sigma value for each data point. The standard error was calculated from the covariance matrix during nonlinear regression and a more rigorous analysis of the variation of the kinetic parameters was accomplished by confidence contour analysis.[42] In this analysis, the lower and upper limits for each parameter were derived from the confidence contours for χ^2 threshold at boundary 0.95.

■ ASSOCIATED CONTENT

Supporting Information

The Supporting Information is available free of charge at https://pubs.acs.org/doi/10.1021/acs.analchem.2c03009.

Experimental details; materials and methods, including protein purification, microfluidic device fabrication, operation of the microfluidic device, and description of the optical platforms; figures including temperature calibration of the microfluidic device; concentration dependence of the aggregation kinetics of Aβ1-42; kinetics of LinB at different temperatures; temperature denaturation experiments; fluorescence signal simulation of LinB kinetics; and global fitting of time-resolved spectra obtained in the microfluidic platform; and tables including statistical analysis of the kinetic constants (PDF)

https://doi.org/10.1021/acs.analchem.2c03009
Anal. Chem. 2022, 94, 16675−16684

AUTHOR INFORMATION

Corresponding Authors

Paolo Arosio − *Institute for Chemical and Bioengineering, ETH Zürich, 8093 Zürich, Switzerland;* orcid.org/0000-0002-2740-1205; Email: paolo.arosio@chem.ethz.ch

Zbynek Prokop − *Loschmidt Laboratories, Department of Experimental Biology and RECETOX, Faculty of Science, Masaryk University, 625 00 Brno, Czech Republic;* orcid.org/0000-0001-9358-4081; Email: zbynek@chemi.muni.cz

Andrew deMello − *Institute for Chemical and Bioengineering, ETH Zürich, 8093 Zürich, Switzerland;* Email: andrew.demello@chem.ethz.ch

Stavros Stavrakis − *Institute for Chemical and Bioengineering, ETH Zürich, 8093 Zürich, Switzerland;* orcid.org/0000-0002-0888-5953; Email: stavros.stavrakis@chem.ethz.ch

Authors

Tianjin Yang − *Institute for Chemical and Bioengineering, ETH Zürich, 8093 Zürich, Switzerland;* Present Address: Department of Biochemistry, University of Zurich, Winterthurerstrasse 190, 8057 Zurich, Switzerland

Alessia Villois − *Institute for Chemical and Bioengineering, ETH Zürich, 8093 Zürich, Switzerland*

Antonín Kunka − *Loschmidt Laboratories, Department of Experimental Biology and RECETOX, Faculty of Science, Masaryk University, 625 00 Brno, Czech Republic; International Clinical Research Center, St. Anne's University Hospital, 656 91 Brno, Czech Republic*

Fulvio Grigolato − *Institute for Chemical and Bioengineering, ETH Zürich, 8093 Zürich, Switzerland*

Complete contact information is available at: https://pubs.acs.org/10.1021/acs.analchem.2c03009

Author Contributions

[⊥]T.Y. and A.V. contributed equally to this work.

Notes

The authors declare no competing financial interest.

ACKNOWLEDGMENTS

The authors acknowledge financial support from the Swiss National Science Foundation (grant no. 205321_17905), the Swiss National Science Foundation (grant no. 205321_176011), and ETH Zurich. They also acknowledge funding from the Czech Ministry of Education (TEAMING CZ.02.1.01/0.0/0.0/17_043/0009632) and from the European Union's Horizon 2020 research and innovation program (TEAMING 857560).

REFERENCES

(1) Yang, W. Y.; Gruebele, M. *Nature* **2003**, *423*, 193−197.
(2) Kintses, B.; Simon, Z.; Gyimesi, M.; Tóth, J.; Jelinek, B.; Niedetzky, C.; Kovács, M.; Málnási-Csizmadia, A. *Biophys. J.* **2006**, *91*, 4605−4610.
(3) Deng, H.; Zhadin, N.; Callender, R. *Biochemistry* **2001**, *40*, 3767−3773.
(4) Kuznetsov, S. V.; Kozlov, A. G.; Lohman, T. M.; Ansari, A. *J. Mol. Biol.* **2006**, *359*, 55−65.
(5) Johnson, K. A.Transient State Enzyme Kinetics. In *Wiley Encyclopedia of Chemical Biology*; John Wiley & Sons, 2007; pp 1−8.
(6) Kubelka, J. *Photochem. Photobiol. Sci.* **2009**, *8*, 499−512.
(7) Callender, R.; Dyer, R. B. *Curr. Opin. Struct. Biol.* **2002**, *12*, 628−633.
(8) Knight, J. B.; Vishwanath, A.; Brody, J. P.; Austin, R. H. *Phys. Rev. Lett.* **1998**, *80*, 3863−3866.
(9) Song, H.; Bringer, M. R.; Tice, J. D.; Gerdts, C. J.; Ismagilov, R. F. *Appl. Phys. Lett.* **2003**, *83*, 4664−4666.
(10) Polinkovsky, M. E.; Gambin, Y.; Banerjee, P. R.; Erickstad, M. J.; Groisman, A.; Deniz, A. A. *Nat. Commun.* **2014**, *5*, No. 5737.
(11) Ebbinghaus, S.; Dhar, A.; McDonald, J. D.; Gruebele, M. *Nat. Methods* **2010**, *7*, 319−323.
(12) Hess, D.; Yang, T.; Stavrakis, S. *Anal. Bioanal. Chem.* **2020**, *412*, 3265−3283.
(13) Hess, D.; Dockalova, V.; Kokkonen, P.; Bednar, D.; Damborsky, J.; DeMello, A.; Prokop, Z.; Stavrakis, S. *Chem* **2021**, *7*, 1066−1079.
(14) Ding, Y.; Howes, P. D.; deMello, A. J. *Anal. Chem.* **2020**, *92*, 132−149.
(15) Song, H.; Ismagilov, R. F. *J. Am. Chem. Soc.* **2003**, *125*, 14613−14619.
(16) Rauk, A. *Chem. Soc. Rev.* **2009**, *38*, 2698−2715.
(17) Serpell, L. C. *Biochim. Biophys. Acta, Mol. Basis Dis.* **2000**, *1502*, 16−30.
(18) Norrild, R. K.; Vettore, N.; Coden, A.; Xue, W.-F.; Buell, A. K. *Biophys. Chem.* **2021**, *271*, No. 106549.
(19) Arosio, P.; Vendruscolo, M.; Dobson, C. M.; Knowles, T. P. *Trends Pharmacol. Sci.* **2014**, *35*, 127−135.
(20) Cohen, S. I. A.; Cukalevski, R.; Michaels, T. C. T.; Šarić, A.; Törnquist, M.; Vendruscolo, M.; Dobson, C. M.; Buell, A. K.; Knowles, T. P. J.; Linse, S. *Nat. Chem.* **2018**, *10*, 523−531.
(21) Meisl, G.; Yang, X.; Hellstrand, E.; Frohm, B.; Kirkegaard, J. B.; Cohen, S. I.; Dobson, C. M.; Linse, S.; Knowles, T. P. *Proc. Natl. Acad. Sci. U.S.A.* **2014**, *111*, 9384−9389.
(22) Koudelakova, T.; Bidmanova, S.; Dvorak, P.; Pavelka, A.; Chaloupkova, R.; Prokop, Z.; Damborsky, J. *Biotechnol. J.* **2013**, *8*, 32−45.
(23) Kokkonen, P.; Koudelakova, T.; Chaloupkova, R.; Daniel, L.; Prokop, Z.; Damborsky, J.Structure-Function Relationships and Engineering of Haloalkane Dehalogenases. In *Aerobic Utilization of Hydrocarbons, Oils, and Lipids*; Rojo, F., Ed.; Springer International Publishing: Cham, 2019; pp 367−387.
(24) Musil, M.; Konegger, H.; Hon, J.; Bednar, D.; Damborsky, J. *ACS Catal.* **2019**, *9*, 1033−1054.
(25) Beerens, K.; Mazurenko, S.; Kunka, A.; Marques, S. M.; Hansen, N.; Musil, M.; Chaloupkova, R.; Waterman, J.; Brezovsky, J.; Bednar, D.; Prokop, Z.; Damborsky, J. *ACS Catal.* **2018**, *8*, 9420−9428.
(26) Brezovsky, J.; Babkova, P.; Degtjarik, O.; Fortova, A.; Gora, A.; Iermak, I.; Rezacova, P.; Dvorak, P.; Smatanova, I. K.; Prokop, Z.; Chaloupkova, R.; Damborsky, J. *ACS Catal.* **2016**, *6*, 7597−7610.
(27) Kazlauskas, R. *Chem. Soc. Rev.* **2018**, *47*, 9026−9045.
(28) Bergasa-Caceres, F.; Rabitz, H. A. *J. Phys. Chem. B.* **2020**, *124*, 8201−8208.
(29) Soto, C.; Pritzkow, S. *Nat. Neurosci.* **2018**, *21*, 1332−1340.
(30) Sanchez-Ruiz, J. M. *Biophys. Chem.* **2010**, *148*, 1−15.
(31) Colón, W.; Church, J.; Sen, J.; Thibeault, J.; Trasatti, H.; Xia, K. *Biochemistry* **2017**, *56*, 6179−6186.
(32) Teale, F. W. J.; Weber, G. *Biochem. J.* **1957**, *65*, 476−482.
(33) LaFerla, F. M.; Green, K. N.; Oddo, S. *Nat. Rev. Neurosci.* **2007**, *8*, 499−509.
(34) Khurana, R.; Coleman, C.; Ionescu-Zanetti, C.; Carter, S. A.; Krishna, V.; Grover, R. K.; Roy, R.; Singh, S. *J. Struct. Biol.* **2005**, *151*, 229−238.
(35) Cohen, S. I. A.; Linse, S.; Luheshi, L. M.; Hellstrand, E.; White, D. A.; Rajah, L.; Otzen, D. E.; Vendruscolo, M.; Dobson, C. M.; Knowles, T. P. J. *Proc. Natl. Acad. Sci. U.S.A.* **2013**, *110*, 9758−9763.
(36) Arosio, P.; Knowles, T. P. J.; Linse, S. *Phys. Chem. Chem. Phys.* **2015**, *17*, 7606−7618.
(37) Arosio, P.; Cukalevski, R.; Frohm, B.; Knowles, T. P. J.; Linse, S. *J. Am. Chem. Soc.* **2014**, *136*, 219−225.

(38) Buell, A. K.; Dhulesia, A.; White, D. A.; Knowles, T. P.; Dobson, C. M.; Welland, M. E. *Angew. Chem., Int. Ed.* **2012**, *51*, 5247−5251.
(39) van Gils, J. H. M.; van Dijk, E.; Peduzzo, A.; Hofmann, A.; Vettore, N.; Schützmann, M. P.; Groth, G.; Mouhib, H.; Otzen, D. E.; Buell, A. K.; Abeln, S. *PLoS Comput. Biol.* **2020**, *16*, No. e1007767.
(40) Vivian, J. T.; Callis, P. R. *Biophys. J.* **2001**, *80*, 2093−2109.
(41) Meadows, M. K.; Sun, X.; Kolesnichenko, I. V.; Hinson, C. M.; Johnson, K. A.; Anslyn, E. V. *Chem. Sci.* **2019**, *10*, 8817−8824.
(42) Johnson, K. A.; Simpson, Z. B.; Blom, T. *Anal. Biochem.* **2009**, *387*, 30−41.
(43) Goldenzweig, A.; Fleishman, S. J. *Annu. Rev. Biochem.* **2018**, *87*, 105−129.
(44) Broom, A.; Ma, S. M.; Xia, K.; Rafalia, H.; Trainor, K.; Colón, W.; Gosavi, S.; Meiering, E. M. *Proc. Natl. Acad. Sci. U.S.A.* **2015**, *112*, 14605−14610.
(45) Buell, A. K.; Dhulesia, A.; White, D. A.; Knowles, T. P. J.; Dobson, C. M.; Welland, M. E. *Angew. Chem., Int. Ed.* **2012**, *51*, 5247−5251.
(46) Johnson, K. A.; Simpson, Z. B.; Blom, T. *Anal. Biochem.* **2009**, *387*, 20−29.

Recommended by ACS

Integrated Microfluidic DNA Storage Platform with Automated Sample Handling and Physical Data Partitioning

Yuan Luo, Xingyu Jiang, *et al.*

SEPTEMBER 15, 2022
ANALYTICAL CHEMISTRY
READ

Two-Layered Microfluidic Devices for High-Throughput Dynamic Analysis of Synthetic Gene Circuits in *E. coli*

Yanhong Sun, Chunxiong Luo, *et al.*

OCTOBER 25, 2022
ACS SYNTHETIC BIOLOGY
READ

Dynamic Reconfiguration of Subcompartment Architectures in Artificial Cells

Greta Zubaite, Yuval Elani, *et al.*

JUNE 13, 2022
ACS NANO
READ

Acoustic Focusing of Protein Crystals for In-Line Monitoring and Up-Concentration during Serial Crystallography

Björn Hammarström, Jonas A. Sellberg, *et al.*

SEPTEMBER 02, 2022
ANALYTICAL CHEMISTRY
READ

Get More Suggestions >

https://doi.org/10.1021/acs.analchem.2c03009
Anal. Chem. 2022, 94, 16675−16684